

## Transition to magnetorotational turbulence in Taylor–Couette flow with imposed azimuthal magnetic field

This content has been downloaded from IOPscience. Please scroll down to see the full text.

2015 New J. Phys. 17 093018

(<http://iopscience.iop.org/1367-2630/17/9/093018>)

View [the table of contents for this issue](#), or go to the [journal homepage](#) for more

Download details:

IP Address: 129.11.22.59

This content was downloaded on 18/09/2015 at 09:47

Please note that [terms and conditions apply](#).



## PAPER

# Transition to magnetorotational turbulence in Taylor–Couette flow with imposed azimuthal magnetic field

A Guseva<sup>1</sup>, A P Willis<sup>2</sup>, R Hollerbach<sup>3</sup> and M Avila<sup>1</sup>

<sup>1</sup> Friedrich-Alexander University Erlangen–Nürnberg, Germany

<sup>2</sup> School of Mathematics and Statistics, University of Sheffield, Sheffield S3 7RH, UK

<sup>3</sup> School of Mathematics, University of Leeds, Leeds LS2 9JT, UK

E-mail: [anna.guseva@fau.de](mailto:anna.guseva@fau.de)

**Keywords:** magnetorotational instability, Taylor–Couette flow, MHD

Supplementary material for this article is available [online](#)

RECEIVED  
11 April 2015

REVISED  
27 July 2015

ACCEPTED FOR PUBLICATION  
12 August 2015

PUBLISHED  
11 September 2015

Content from this work  
may be used under the  
terms of the [Creative  
Commons Attribution 3.0  
licence](#).

Any further distribution of  
this work must maintain  
attribution to the  
author(s) and the title of  
the work, journal citation  
and DOI.



## Abstract

The magnetorotational instability (MRI) is thought to be a powerful source of turbulence and momentum transport in astrophysical accretion discs, but obtaining observational evidence of its operation is challenging. Recently, laboratory experiments of Taylor–Couette flow with externally imposed axial and azimuthal magnetic fields have revealed the kinematic and dynamic properties of the MRI close to the instability onset. While good agreement was found with linear stability analyses, little is known about the transition to turbulence and transport properties of the MRI. We here report on a numerical investigation of the MRI with an imposed azimuthal magnetic field. We show that the laminar Taylor–Couette flow becomes unstable to a wave rotating in the azimuthal direction and standing in the axial direction via a supercritical Hopf bifurcation. Subsequently, the flow features a catastrophic transition to spatio-temporal defects which is mediated by a subcritical subharmonic Hopf bifurcation. Our results are in qualitative agreement with the PROMISE experiment and dramatically extend their realizable parameter range. We find that as the Reynolds number increases defects accumulate and grow into turbulence, yet the momentum transport scales weakly.

## 1. Introduction

The magnetorotational instability (MRI) is of great importance in astrophysics. First discovered by Velikhov [1] in 1959, it remained unnoticed until 1991 when Balbus and Hawley [2] realized its application to accretion disc theory. Accretion discs are astrophysical systems that consist of ionized gas and dust orbiting a massive body. Planets and stars are formed from this initially dispersed matter. The physical mechanism of accretion is straightforward: a parcel of viscous fluid in the differentially rotating disc loses its angular momentum over time and falls onto the central object. To explain the astrophysically observed rates of accretion, however, one must assume a turbulent transport of angular momentum in the outward direction [3]. In so-called Keplerian discs the angular velocity profile of gas follows the law

$$\Omega \sim r^{-3/2}, \quad (1)$$

which is hydrodynamically stable according to the Rayleigh criterion for rotating fluids [4]:

$$\frac{d(r^2\Omega)^2}{dr} > 0 \quad \text{for stability.} \quad (2)$$

Ionized accretion discs, however, are necessarily magnetized and the MRI may still act in rotating flows, provided the angular velocity decreases with radius, which is true of Keplerian flows (1).

The growth rates of the MRI and the parameter ranges in which it acts were determined in several linear analyses [2, 5–8], but these do not provide information about the flow structure and scaling of angular momentum transport after nonlinear saturation. In the last two decades there has been a great deal of numerical

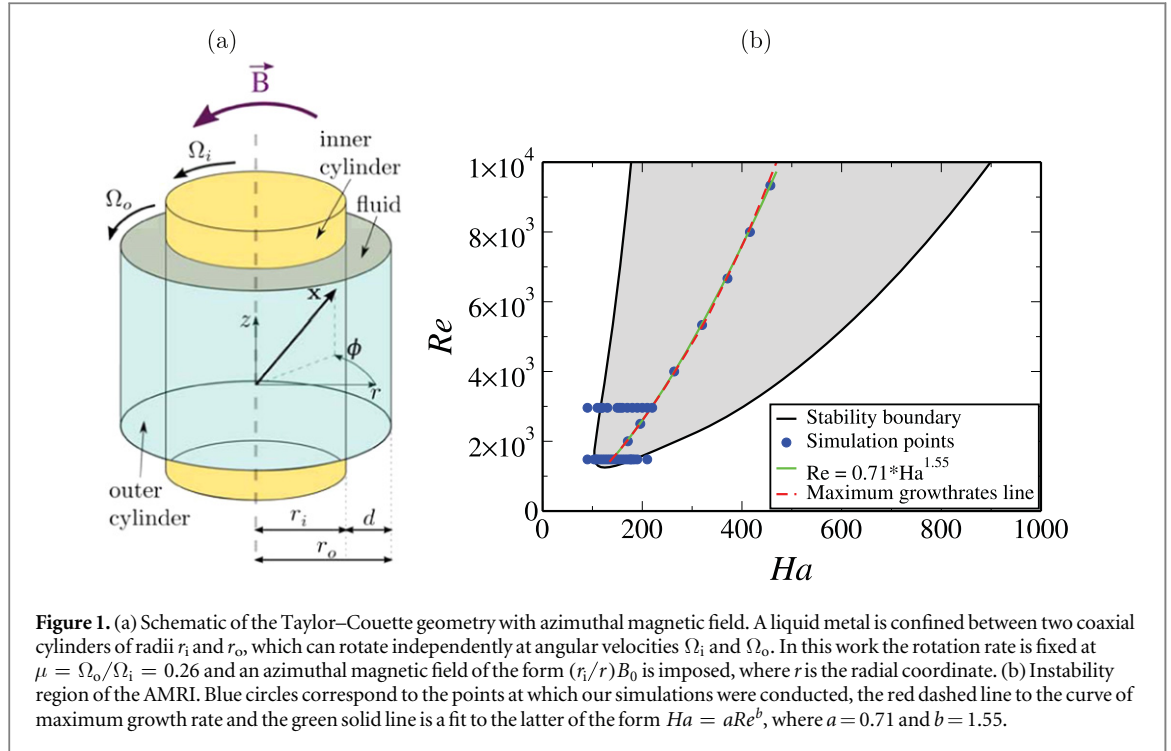


**Figure 1.** (a) Schematic of the Taylor–Couette geometry with azimuthal magnetic field. A liquid metal is confined between two coaxial cylinders of radii  $r_i$  and  $r_o$ , which can rotate independently at angular velocities  $\Omega_i$  and  $\Omega_o$ . In this work the rotation rate is fixed at  $\mu = \Omega_o/\Omega_i = 0.26$  and an azimuthal magnetic field of the form  $(r_i/r)B_0$  is imposed, where  $r$  is the radial coordinate. (b) Instability region of the AMRI. Blue circles correspond to the points at which our simulations were conducted, the red dashed line to the curve of maximum growth rate and the green solid line is a fit to the latter of the form  $Ha = aRe^b$ , where  $a = 0.71$  and  $b = 1.55$ .

**Table 1.** Dimensionless parameters of the magnetohydrodynamic Taylor–Couette problem.

Abbrev.	Parameter	Definition	Range
$\delta$	Radius ratio	$r_i/r_o$	0.5
$\alpha$	Axial wavenumber (geometrical parameter)	$2\pi/L_z$	0.5–4.5
$\mu$	Angular velocity ratio	$\Omega_o/\Omega_i$	0.26
$Pm$	Magnetic Prandtl number	$\nu/\eta$	$1.4 \times 10^{-6}$
$Re$	Reynolds numbers of inner cylinder	$\Omega_i r_i d/\nu$	1480–9333
$Ha$	Hartmann number	$B_0 d / \left( \frac{\sigma}{\rho\nu} \right)^{1/2}$	90–457

work concerned with the nonlinear properties of the MRI. Simulations are usually performed with the shearing sheet approximation, which is a local model of an accretion disc with shear-periodic boundary conditions in the radial direction [6]. The main disadvantage of this model is the influence of boundary conditions on the geometry of the observed modes and transport scaling. In particular, the length of the computational box fixes the modes that appear and determines their nonlinear saturation. As it is not clear how the length should be selected, the interpretation of the transport scaling becomes quite involved [9].

These theoretical results and numerical simulations inspired physicists to realize the MRI in laboratory experiments. In 2001 Ji *et al* [10] and Rüdiger and Zhang [11] independently suggested the possibility of directly observing magnetorotational instabilities in a cylindrical vessel made of two co-axial and independently rotating cylinders containing a liquid metal alloy (see figure 1(a)). The standard form of the MRI (SMRI), which they proposed, emerges when a purely axial magnetic field is imposed, but this has not yet been achieved in experiments. The difficulty is that liquid metals have very small magnetic Prandtl numbers (e.g.  $Pm \sim 10^{-6}$  for gallium alloys), leading in this case to very large Reynolds numbers ( $Re \gtrsim 10^7$ ) necessary to observe the SMRI (see table 1 for the definitions of  $Re$  and  $Pm$ ). In fact, such high Reynolds numbers have never been achieved even for non-magnetic Taylor–Couette flows. A further difficulty of Taylor–Couette experiments in the quasi-Keplerian regime arises because of Ekman vortices that arise adjacent to the endplates. Unless a very specific endplate arrangement is used, the Ekman vortices extend deep into the flow and even at moderate Reynolds number the basic Couette flow cannot be obtained experimentally [12]. The resulting velocity profiles are no longer quasi-Keplerian and hydrodynamic instabilities render the flow turbulent even in the absence of magnetic fields [13, 14].

Hollerbach and Rüdiger [7] proposed instead a combination of axial and azimuthal magnetic fields, giving rise to the helical MRI (HMRI) at much lower  $Re \sim 10^3$  for Hartmann numbers  $Ha \sim 10$  (see table 1 for the definition of  $Ha$ ). This was successfully observed [15, 16] in the Potsdam-ROsendorf magnetic instability

experiment (PROMISE) facility. Both the SMRI and HMRI consist of axisymmetric toroidal vortices, which are stationary for the former but travel axially for the latter. Hollerbach *et al* [8] realized that although a purely azimuthal magnetic field does not yield any axisymmetric instabilities, non-axisymmetric modes can be destabilized. The resulting azimuthal MRI (AMRI) arises in Taylor–Couette flow at  $Re \sim 10^3$  for  $Ha \sim 10^2$  [8], and a recent upgrade of the PROMISE power supply made its experimental observation possible [17]. In PROMISE the endplates are split into two parts and the inner (outer) one is attached to the inner (outer) cylinder. Although this configuration is acceptable at  $Re \leq 3000$ , as studied experimentally, endplate effects become dominant at larger  $Re$ . Because of this, and of the practical impossibility of generating a purely azimuthal magnetic field experimentally, it is challenging to actually identify the AMRI modes in the experimental data unambiguously (see [17]).

Despite this recent experimental progress in realizing magnetorotational instabilities in the laboratory, little is known about their bifurcation scenario, transition to turbulence and transport properties as  $Re$  increases. In this work we address these points for the AMRI. We perform direct numerical simulations of the coupled induction and Navier–Stokes equations using axially periodic boundary conditions, thereby avoiding undesired endplate effects and focusing on the features intrinsic to the AMRI. We find that the laminar quasi-Keplerian flow becomes unstable to a wave rotating in the azimuthal direction and standing in the axial direction. Subsequently, we identify a new bifurcation scenario giving rise to spatio-temporal defects via a subcritical subharmonic Hopf bifurcation. As the Reynolds number is further increased, the flow becomes turbulent and outward momentum transport is enhanced, albeit at a weak rate. The results are in good qualitative agreement with the PROMISE observations [17] and substantially extend the parameter range explored experimentally.

## 2. Governing equations

We consider an incompressible viscous liquid metal that is sheared between two independently rotating cylinders of radii  $r_i$  (inner) and  $r_o$  (outer). The angular velocity of the cylinders are  $\Omega_i$  and  $\Omega_o$ , respectively, and an external azimuthal magnetic field  $(r_i/r)B_0$ , where  $r$  is the radial coordinate, is imposed. The relevant fluid properties are the electrical conductivity  $\sigma$ , the kinematic viscosity  $\nu$ , the density  $\rho$  and the magnetic diffusivity  $\eta$ . The velocity field  $\mathbf{u}$  is determined by the Navier–Stokes equations (3), whereas the magnetic field  $\mathbf{B}$  is determined by the induction equation (4), which represents a combination of the laws of Ampere, Faraday, and Ohm. The equations were rendered dimensionless by using the gap between cylinders  $d = r_o - r_i$  for length,  $d^2/\nu$  for time, and  $B_0$  for the magnetic field. In dimensionless form they read

$$(\partial_t + \mathbf{v} \cdot \nabla)\mathbf{v} = -\nabla p + \nabla^2 \mathbf{v} + \frac{Ha^2}{Pm}(\nabla \times \mathbf{B}) \times \mathbf{B}, \quad (3)$$

$$\left(\partial_t - \frac{1}{Pm}\nabla^2\right)\mathbf{B} = \nabla \times (\mathbf{v} \times \mathbf{B}), \quad (4)$$

together with  $\nabla \cdot \mathbf{v} = \nabla \cdot \mathbf{B} = 0$ . Here  $p$  is the pressure,  $Ha$  the Hartmann number, and  $Pm$  the magnetic Prandtl number. The dimensionless parameters of the system are specified in table 1. Following the PROMISE experiment [17], we use a magnetic Prandtl number of  $Pm = 1.4 \times 10^{-6}$  (corresponding to the alloy  $\text{Ga}^{67}\text{In}^{20.5}\text{Sn}^{12.5}$ ), a radius-ratio of  $\delta = 0.5$  and a rotation-ratio of  $\mu = 0.26$ . This places the velocity profile in the quasi-Keplerian regime, for which the angular velocity decreases radially, whereas the angular momentum increases, i.e.  $\delta^2 < \mu < 1$ .

### 2.1. Boundary conditions

We employ cylindrical coordinates  $(r, \phi, z) \in [r_i, r_o] \times [0, 2\pi] \times [0, L_z]$ , for which the no-slip velocity boundary conditions at the cylinders read

$$u_\phi(r_i, \phi, z) = Re, \quad u_\phi(r_o, \phi, z) = \mu Re. \quad (5)$$

Periodicity in the axial direction is imposed with basic length  $L_z$ . The background circular Couette flow  $\mathbf{V} = V(r)\mathbf{e}_\phi$  is a solution to the equations and boundary conditions given by

$$V(r) = \frac{1}{1 + \delta} \left[ \left( \frac{\mu}{\delta} Re - \delta Re \right) r + \frac{\delta}{(1 - \delta)^2} (Re - \mu Re) \frac{1}{r} \right]. \quad (6)$$

The magnetic field is also assumed to be periodic in the axial direction. In the radial direction the boundary condition depends on the material of the cylinders. Typically two idealized cases are considered in the MRI problem: insulating and conducting cylinders. These lead to slightly different results, as theoretically demonstrated by Chandrasekhar [18]. However, the difference is not great, and here we will consider only the case of insulating boundaries. Assuming the Fourier expansion for each variable

$$A = \sum_{|k| < K} \sum_{|m| < M} A_{k,m}(r) \exp[i(\alpha kz + m\phi)], \quad (7)$$

one obtains the following boundary conditions for  $\mathbf{B}$ :

For case  $k = m = 0$ :

$$B_\theta = B_z = 0. \quad (8)$$

Case  $k = 0, m \neq 0$ :

$$B_r \pm iB_\theta = 0, \quad B_z = 0 \quad (+\text{on } r_1, -\text{on } r_0). \quad (9)$$

Case  $k \neq 0$ :

$$B_r + i \frac{\mathcal{B}'_m(\alpha k R)}{\mathcal{B}_m(\alpha k R)} B_z = 0, \quad \alpha k B_\theta - \frac{m}{r} B_z = 0, \quad (10)$$

where  $\mathcal{B}_m(x)$  denotes the modified Bessel function  $I_m(x)$  for  $r = r_1$  and  $K_m(x)$  for  $r = r_0$ , and  $\mathcal{B}'_m = \partial_x \mathcal{B}_m$ . See Willis and Barenghi [19] for a detailed derivation.

## 2.2. Brief remarks on symmetries of rotating magnetohydrodynamic flows

The basic circular Couette flow (6) has  $\text{SO}(2) \times \text{O}(2)$  symmetry, where  $\text{SO}(2)$  represents the rotational symmetry in the azimuthal direction. In the axial direction the group  $\text{O}(2)$  may be written as  $\text{O}(2) = Z_2 \times \text{SO}(2)$ , where  $Z_2$  is a reflection (up–down symmetry) and  $\text{SO}(2)$  the translational symmetry in the  $z$  direction. The presence of purely axial or purely azimuthal imposed magnetic field does not change the symmetry group of the system. Hence if the primary instability is a Hopf bifurcation the resulting states can be either standing or traveling waves (TWs) in the axial direction [20]. By contrast, a combined helical magnetic field breaks the reflection symmetry and only TWs can be observed [21]. Finally, if the bifurcating solution is non-axisymmetric, as in the AMRI, this will generically be a rotating wave in the azimuthal direction.

## 3. Numerical method

In the numerical simulations only the deviation from the basic flow  $\mathbf{u} = \mathbf{v} - \mathbf{V}$  is computed. Its governing equations read

$$(\partial_t - \nabla^2) \mathbf{u} = \mathbf{N} - \nabla p, \quad \nabla \cdot \mathbf{u} = 0, \quad (11)$$

which are supplemented with homogeneous boundary conditions  $\mathbf{u} = \mathbf{0}$ . Here  $\mathbf{N}$  stands for the nonlinear term in the Navier–Stokes equations (3), which contains the advective terms and the Lorentz force:

$$\begin{aligned} \mathbf{N} &= \mathbf{u} \times (\nabla \times \mathbf{u}) - (\mathbf{V} \cdot \nabla) \mathbf{u} - (\mathbf{u} \cdot \nabla) \mathbf{V} + \frac{Q}{Pm} (\nabla \times \mathbf{B}) \times \mathbf{B} \\ &= \mathbf{u} \times (\nabla \times \mathbf{u}) - (V/r) \partial_\phi \mathbf{u} + (2V/r) u_\phi \mathbf{e}_r - u_r (1 + \partial_r) V \mathbf{e}_\phi + \frac{Q}{Pm} (\nabla \times \mathbf{B}) \times \mathbf{B}. \end{aligned} \quad (12)$$

Spatial discretization is accomplished via the Fourier expansion in the azimuthal and axial directions (7), and as the variables are real, their Fourier coefficients satisfy the property  $A_{k,m} = A_{-k,-m}^*$ , where  $A^*$  denotes the complex conjugate.

The pseudospectral Fourier method is the most efficient choice for periodic boundary conditions. Because of their great accuracy at low resolutions, spectral methods have also been used to discretize the hydromagnetic Taylor–Couette flow problem in the radial direction [19, 22]. In these works the Chebyshev collocation method was chosen because of its simplicity. Nevertheless its computational and storage costs scale as  $\mathcal{O}(N^2)$ , where  $N$  is the number of radial points, making computations at large Reynolds number impractical. Petrov–Galerkin formulations reduce the cost to  $\mathcal{O}(N)$  and have been also used in hydrodynamic Taylor–Couette flows [23, 24]. However, the treatment of the radial boundary conditions becomes very cumbersome for the magnetic field. We here use the finite-difference method in the radial direction. Radial derivatives are calculated using 9-point stencils to  $(9 - j)$ th order, where  $j$  is the order of the derivative. This results in banded matrices with associated  $\mathcal{O}(N)$  cost, while providing excellent accuracy. Reference [25] provides a more thorough discussion of these computational issues and the accuracy of the finite-difference method applied to hydrodynamic Taylor–Couette flow.

A second-order scheme is applied to the time discretization  $t^q = q \Delta t$ , based on the implicit Crank–Nicolson method. Applying this method to the Navier–Stokes equations, we find

$$(1/\Delta t - \nabla^2) \mathbf{u}^{q+1} = (1/\Delta t + \nabla^2) \mathbf{u}^q + \mathbf{N}^{q+\frac{1}{2}} - \nabla p, \quad \nabla^2 p = \nabla \cdot \mathbf{N}^{q+\frac{1}{2}}, \quad (13)$$

where  $\mathbf{N}^{q+\frac{1}{2}}$  is an estimate for the nonlinear terms (Euler predictor, Crank–Nicolson corrector). In cylindrical coordinates the  $r$ - and  $\phi$ -components of the Laplacian operator couples the two components, and for a Fourier decomposition they are complex operators. Programming complexity and computational cost of inversion for  $u_r^{q+1}$  and  $u_\phi^{q+1}$  can be reduced, however, by considering

$$u_\pm = u_r \pm i u_\phi, \quad \text{i.e. } u_r = \frac{1}{2}(u_+ + u_-), \quad u_\phi = -\frac{i}{2}(u_+ - u_-), \quad (14)$$

where the  $\pm$  are taken respectively. The equations governing these components separate and the Laplacian operator is now real ( $\partial_\phi \rightarrow im$ ),

$$\left(\partial_t - \nabla_\pm^2\right)u_\pm = N_\pm - (\nabla p)_\pm, \quad \nabla_\pm^2 = \nabla^2 - \frac{1}{r^2} \pm \frac{i}{r^2} \partial_\phi. \quad (15)$$

### 3.1. Influence-matrix method

The natural approach to solving (13) is to invert for  $p$  and then for  $\mathbf{u}^{q+1}$ . All the boundary conditions are on  $\mathbf{u}^{q+1}$ , however, there are none on  $p$ , and it is well known that primitive variable formulations are subject to loss of temporal order if inappropriate boundary conditions are enforced on  $p$  [26]. For the magnetic field, there appear at first sight to be too few boundary conditions, and further, the components of  $\mathbf{B}$  are coupled in the boundary condition. It is shown here that the influence-matrix method resolves these issues, the appropriate boundary conditions can be satisfied to machine precision, and temporal order is retained. We show first how the method is applied for time integration of the velocity field, similar to [27]. An analogous approach is applied to the magnetic field.

#### 3.1.1. Method for the velocity field

We write the time-discretized Navier–Stokes equations (13) in the form

$$\begin{cases} X\mathbf{u}^{q+1} = Y\mathbf{u}^q + \mathbf{N}^{q+\frac{1}{2}} - \nabla p, \\ \nabla^2 p = \nabla \cdot (Y\mathbf{u}^q + \mathbf{N}^{q+\frac{1}{2}}), \end{cases} \quad (16)$$

where  $q$  denotes time  $t_q$ . This form is sixth order in  $r$  for  $\mathbf{u}^{q+1}$  and second order for  $p$ , without the solenoidal condition explicitly imposed. In principle this system should be inverted simultaneously for  $p$  and  $\mathbf{u}^{q+1}$  with boundary conditions  $\mathbf{u}^{q+1} = \mathbf{0}$  and  $\nabla \cdot \mathbf{u}^{q+1} = \mathbf{0}$ . In practice it would be preferable to invert for  $p$  first then for  $\mathbf{u}^{q+1}$ , but the boundary conditions do not involve  $p$  directly. Note that the  $Y\mathbf{u}^q$  term has been included in the right-hand side of the pressure–Poisson equation, so that it corresponds precisely to the divergence of the equation for  $\mathbf{u}^{q+1}$ . This ensures that any non-zero divergence in the initial condition is projected out after a single time-step. We split the system (16) into the ‘bulk’ solution,  $\{\bar{\mathbf{u}}, \bar{p}\}$ ,

$$\begin{cases} X\bar{\mathbf{u}} = Y\mathbf{u}^q + \mathbf{N}^{q+\frac{1}{2}} - \nabla \bar{p}, \\ \nabla^2 \bar{p} = \nabla \cdot (Y\mathbf{u}^q + \mathbf{N}^{q+\frac{1}{2}}), \end{cases} \quad (17)$$

with boundary conditions  $\bar{\mathbf{u}} = \mathbf{0}$  and  $\partial_r \bar{p} = 0$ , and the auxiliary systems

$$\begin{cases} X\mathbf{u}' = -\nabla p', \\ \nabla^2 p' = 0, \end{cases} \quad (18)$$

with two sets of boundary conditions,  $\mathbf{u}' = \mathbf{0}$  with  $\partial_r p' = \{0, 1\}$  and  $\{1, 0\}$  on  $r = \{r_i, r_o\}$ , and

$$\begin{cases} X\mathbf{u}' = \mathbf{0}, \end{cases} \quad (19)$$

with boundary conditions  $u'_+ = \{0, 1\}$ ,  $u'_- = \{0, 1\}$ ,  $u'_z = \{0, i\}$  and similarly their reversed versions on  $\{r_i, r_o\}$ . These dashed functions may be precomputed, and will be used to correct the approximate boundary conditions used to calculate  $\bar{\mathbf{u}}$  and  $\bar{p} = 0$ .

The system (18) provides, with the two boundary conditions, two linearly independent functions  $\mathbf{u}'_j$  that may be added to  $\bar{\mathbf{u}}$  without altering the right-hand side in (17). Similarly the system (19) provides a further six functions. The superposition

$$\mathbf{u}^{q+1} = \bar{\mathbf{u}} + \sum_{j=1}^8 a_j \mathbf{u}'_j \quad (20)$$

may be formed in order to satisfy the eight original boundary conditions,  $\mathbf{u}^{q+1} = \mathbf{0}$  and  $\nabla \cdot \mathbf{u}^{q+1} = \mathbf{0}$  on  $r = \{r_i, r_o\}$ . Substituting (20) into the boundary conditions, they may be written

$$A\mathbf{a} = -\mathbf{g}(\bar{\mathbf{u}}), \quad (21)$$

where  $A = A(\mathbf{g}(\mathbf{u}'))$  is an  $8 \times 8$  matrix. The appropriate coefficients required to satisfy the boundary conditions are thereby recovered from the solution of this small system for  $\mathbf{a}$ . The error in the boundary conditions  $g_j(\mathbf{u}^{q+1})$  using the influence-matrix technique is at the level of the machine precision.

The auxiliary functions  $u'_j(r)$ , the matrix  $A$  and its inverse may all be precomputed, and the boundary conditions for  $\mathbf{u}'$  have been chosen so that  $u'_\pm$  are purely real,  $u'_z$  is purely imaginary, and  $A$  is real. For each timestep, this application of the influence matrix technique requires only evaluation of the deviation from the boundary condition, multiplication by an  $8 \times 8$  real matrix, and the addition of four functions to each component of  $\mathbf{u}$ , each either purely real or purely imaginary. Compared to the evaluation of nonlinear terms, the computational overhead is negligible.

### 3.1.2. Method for the magnetic field

Consider the induction equation (4) time-stepped without  $\nabla \cdot \mathbf{B} = 0$  enforced. Evolution of  $\psi = \nabla \cdot \mathbf{B}$  is then governed by the divergence of (4),

$$\partial_t \psi = \frac{1}{Pm} \nabla^2 \psi. \quad (22)$$

In addition to the boundary conditions derived in [19], the condition  $\psi = 0$  must be satisfied on the boundary to avoid introduction of divergence into the domain. Then (4) has the appropriate number of boundary conditions, and  $\psi = \nabla \cdot \mathbf{B}$  should remain zero for a solenoidal initial condition.

To prevent accumulation of divergence from artificial internal sources, i.e. discretization error, it is commonplace to introduce an artificial pressure  $\Pi$  [28]. The discretized system is then as in (16) where one reads  $\mathbf{B}$  for  $\mathbf{u}$  and  $\Pi$  for  $p$ . The boundary condition for  $\Pi$  is any choice such that, when one computes  $\Pi$  for a given  $\mathbf{B}^q$ , it is found to be constant when  $\nabla \cdot \mathbf{B}^q = \mathbf{0}$  [29]. The choice  $\partial_r \Pi = 0$  is applied here. When comparing with the problem for the velocity, here the difficulty is not the coupling of the boundary condition for  $\mathbf{B}$  with  $\Pi$ , but between the components of  $\mathbf{B}$  at an insulating boundary.

Here the system is split as in (17) for the ‘bulk’ solution, with approximate boundary condition  $\bar{\mathbf{B}} = \mathbf{B}^q$  on  $\{r_i, r_o\}$ . This is then corrected precisely via the influence matrix requiring only the simple auxiliary system

$$X\mathbf{B}' = \mathbf{0}, \quad (23)$$

with boundary conditions  $B'_\pm = \{0, 1\}$  or  $\{1, 0\}$  and  $B'_z = \{0, i\}$  or  $\{i, 0\}$  on  $\{r_i, r_o\}$ .

Problem (23) separates for the three components, which, with the two boundary condition options for each, provides six functions  $B'_j(r)$ . The correction is then

$$\mathbf{B}^{q+1} = \bar{\mathbf{B}} + \sum_{j=1}^6 a_j \mathbf{B}'_j. \quad (24)$$

Let  $g_j(\mathbf{B}) = 0$  denote the insulating boundary conditions and solenoidal condition evaluated at  $r_i$  and  $r_o$ . Substituting (24) into the boundary conditions, they may be written  $A\mathbf{a} = -\mathbf{g}(\bar{\mathbf{B}})$ , where  $A = A(\mathbf{g}(\mathbf{B}'))$  is a  $6 \times 6$  matrix. The appropriate coefficients required to satisfy the boundary conditions are recovered from solution of this small system for  $\mathbf{a}$ .

Again, the auxiliary functions  $B'_j(r)$ , the matrix  $A$  and its inverse may be precomputed, and the boundary conditions for  $\mathbf{B}'$  have been chosen so that  $B'_\pm$  are purely real,  $B'_z$  is purely imaginary, and  $A$  is real. At the end of the timestep, the solution is solenoidal and satisfies the boundary conditions to machine precision.

## 3.2. Implementation notes and parallelization

The Taylor–Couette flow code was written in Fortran90. Nonlinear terms are evaluated using the pseudo-spectral method and are de-aliased using the 3/2 rule. The Fourier transforms are performed with the FFTW3 library [30] and matrix and vector operations are performed with BLAS [31]. Each predictor–corrector iteration involves the solution of banded linear systems with forward–backward substitution using banded LU-factorizations that are precomputed prior to time-stepping. These operations are performed with LAPACK [32]. The code was parallelized so that data is split over the Fourier harmonics for the linear parts of the code: evaluating curls, gradients and matrix inversions for the time-stepping (these linear operations do not couple modes). Here all radial points for a particular mode are located on the same processor; separate modes may be located on separate processors. Data is split radially when calculating Fourier transforms and when evaluating products in real space (nonlinear term of the equations). The bulk of communication between processors occurs during the data transposes.

### 3.3. Numerical validation

The code was validated against several published linear stability results, as well as three-dimensional nonlinear simulations of the coupled induction and Navier–Stokes equations. We tested the inductionless limit  $Pm = 0$  and finite  $Pm$ , obtaining excellent agreement in all cases.

#### 3.3.1. Linear stability of Couette flow subject to magnetic fields

Linear instabilities were detected in the calculations by monitoring the kinetic energy of the deviation from circular Couette flow after introduction of a small disturbance. In the linear regime we write

$$u' \sim \exp(\lambda t + i[kz + m\phi]), \quad E \sim |u'|^2 \sim \exp(2\sigma t),$$

where  $\lambda = \sigma + i\omega$  is a complex number; the imaginary part  $\omega$  is the oscillation frequency and the real part  $\sigma$  the growth rate of the dominant perturbation. The latter is readily extracted from the relationship  $\log(E) \sim 2\sigma t$ .

We first reproduced the classical results of Roberts [33], who considered the inductionless limit  $Pm = 0$  for narrow gap geometry  $\delta = 0.95$  and stationary outer cylinder. For a Hartmann number of  $Ha = 5.477$  he obtained a critical Reynolds number of  $Re_c = 281.05$  with associated critical axial wavenumber of  $\alpha_c = 2.69$  and  $m = 0$ . In our simulations we fixed  $\alpha = \alpha_c$  and obtained  $Re_c = 281.055$  using  $N = 33$  radial points. For finite magnetic Prandtl number  $Pm = 1$  we reproduced the results of Willis and Barenghi [34] for wide gap  $\delta = 0.5$  and stationary outer cylinder. For  $Ha = 39$ , and  $\alpha = 2.4$  and  $m = 0$  they found  $Re_c = 60.5$ , which is in good agreement with our result ( $Re_c = 60.3$ ). In order to test the azimuthal magnetic field we reproduced recent results of Hollerbach *et al* [8] for the AMRI. For example at  $Pm = 0$ ,  $Ha = 316$ ,  $Re = 1000$ ,  $\delta = 0.5$  and  $\mu = 0.26$ , they obtained  $\sigma = -78.6$  for wavenumbers  $\alpha = 7.17$  and  $m = 1$ , which is in very good agreement with our value  $\sigma = -78.7$ .

#### 3.3.2. Nonlinear simulations

Willis and Barenghi [35] explored dynamo action in Taylor–Couette flow. They first solved the Navier–Stokes equations in the absence of magnetic field and subsequently applied a small magnetic disturbance to test whether it grew into a dynamo. In the axisymmetric Taylor-vortex regime axisymmetric magnetic fields were found to decay, in accordance with Cowling’s anti-dynamo theorem. Non-axisymmetric magnetic fields may be excited, however, and for  $Re = 136.4$ ,  $\delta = 0.5$ ,  $Pm = 2$ ,  $\alpha = 1.57$  and stationary outer cylinder they observed that the magnetic disturbance grows for  $m = 1$  ( $\sigma_{B,m=1} \approx 0.2$ , leading to dynamo action), whereas it decays for  $m = 2$  ( $\sigma_{B,m=2} \approx -1.4$ ). We reproduced this setting using  $N = 41$ ,  $K = 16$  and  $M = 12$  and obtained  $\sigma_{B,m=1} \approx 0.16$  and  $\sigma_{B,m=2} \approx -1.42$ , in good agreement with [35].

Finally, we compared results of the axisymmetric HMRI (helical field  $\mathbf{B} = B_0(\mathbf{e}_z + \gamma\mathbf{e}_\phi)$ ) obtained with the spectral code of Hollerbach [22]. A typical diagnostic quantity is the torque at the cylinders

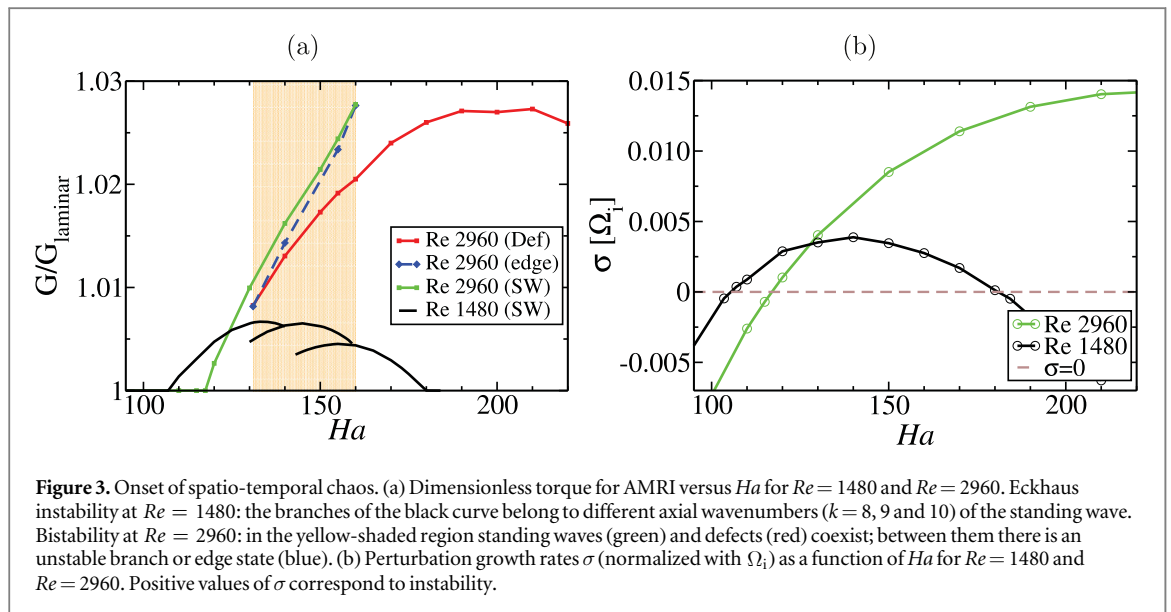
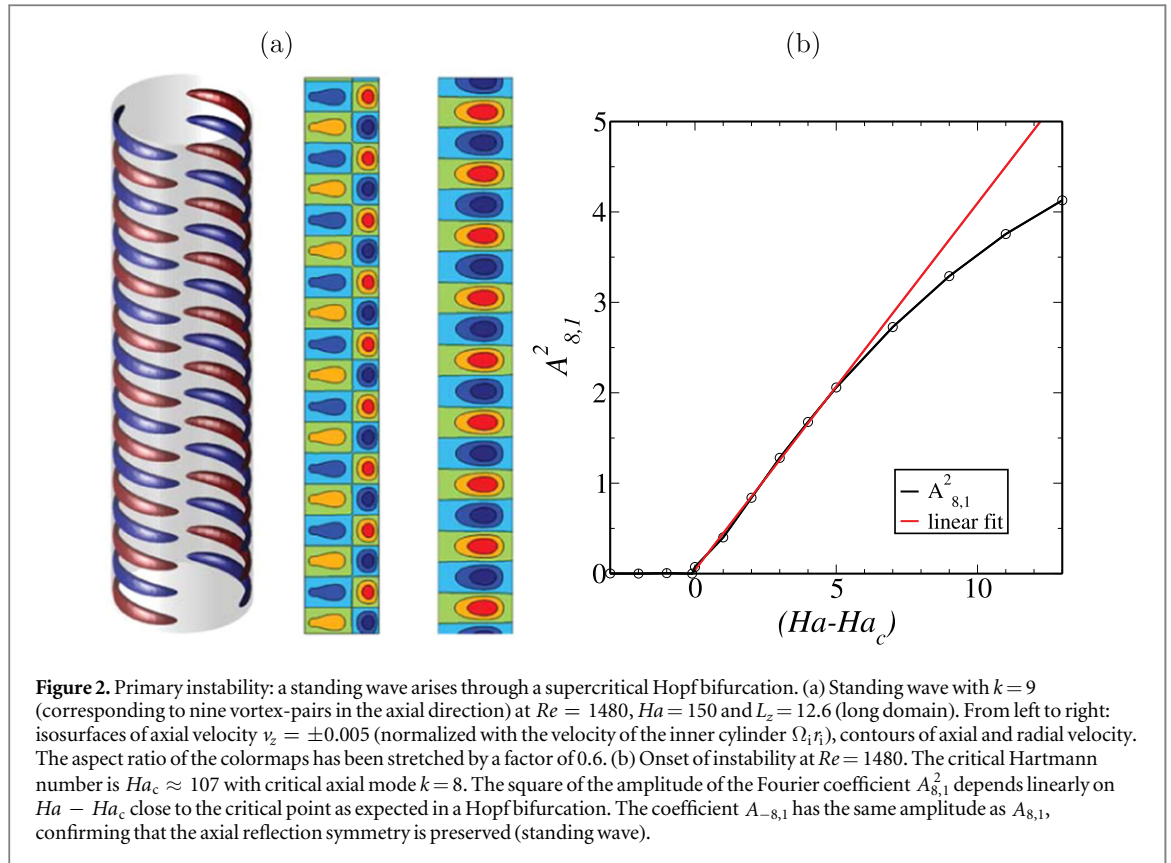
$$G \sim -2\pi r^3 \frac{\partial}{\partial r} \left[ \frac{u_\phi}{r} \right] \sim 2\pi r^2 \left[ \frac{u_\phi}{r} - \partial_r u_\phi \right]. \quad (25)$$

The laminar flow torque will be used as a scale, so that the dimensionless ratio  $G/G_{\text{laminar}}$  measures the intensity of angular momentum transfer relative to laminar flow. We choose the parameters  $Re = 300$ ,  $Ha = 10$ ,  $\delta = 0.5$ ,  $\gamma = 2$ ,  $\alpha = 0.314$ , which are well into the nonlinear regime. After nonlinear saturation the dimensionless torque on the cylinders obtained with our code for  $N = 81$  and  $K = 192$  was  $G/G_{\text{laminar}} = 1.4122$ , which is in excellent agreement with the code of Hollerbach ( $G/G_{\text{laminar}} = 1.4123$ ).

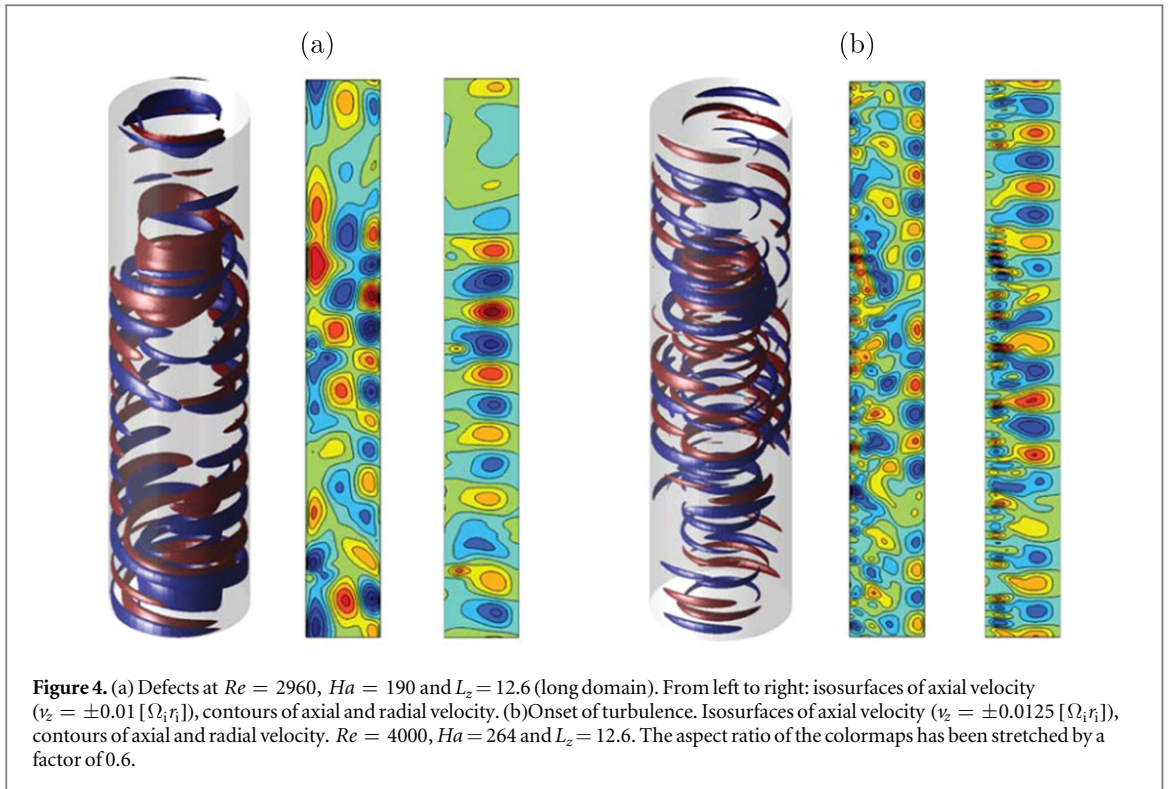
## 4. Primary instability: standing waves (SWs)

In the experiments of Seilmayer *et al* [17] the AMRI was explored near the onset of instability for two different Reynolds numbers  $Re = 1480$  and  $2960$ , and Hartmann numbers in the range  $Ha \in [0, 160]$ . The experiments have an aspect-ratio of 10. Here we selected a periodic domain of length  $L_z = 12.6$ , and initialized the simulations by disturbing all Fourier modes with the same amplitude, thus allowing the axial wavenumber to be naturally selected. Because of the symmetries (see section 2.2), two different Hopf-bifurcation scenarios are possible [21]. In the first one, the  $z$ -reflection symmetry is broken and depending on the initial conditions either upward TWs (with  $k > 0$  modes) or downward TWs (with  $k < 0$  modes) may be observed. In the second scenario, the  $z$ -reflection symmetry is preserved and a SW emerges. This is a combination of upward and downward TWs for which positive and negative  $k$  modes are in phase and have exactly the same amplitude. In both scenarios waves rotate in the azimuthal direction.

We found that at  $Re = 1480$  the circular Couette flow (6) becomes unstable at  $Ha_c = 107$ . The emerging pattern is a SW with dominant mode  $(k, m) = (\pm 8, 1)$ , so that eight pairs of vortices fit in the domain. Figure 2(b) shows the square of the amplitude of the complex Fourier coefficient  $A_{8,1}$  for increasing  $Ha$ . As



expected in a Hopf bifurcation,  $A_{k,m}^2 \propto Ha - Ha_c$  near the onset of instability, and this relationship holds up to  $Ha \approx 112$ . The vortex arrangement of the SW at  $Ha = 150$  is shown in the flow snapshot of figure 2(a). In this case the mode  $k = 9$  was naturally selected. Thus the dominant axial wavenumber depends on  $Ha$  because of the Eckhaus instability, as also observed in hydrodynamic Taylor–Couette flow [36]. The torque changes respectively with axial wavenumber (black curve on the figure 3(a)), so at the same parameter value states with different wavenumber and torque can be realized depending on the initial conditions. Further increasing  $Ha$  the instability is gradually damped until it disappears at  $Ha \approx 175$ . Over the whole Hartmann range the additional torque due to the SW never exceeds 1% of the laminar flow (see figure 3(a)), indicating very weak transport of



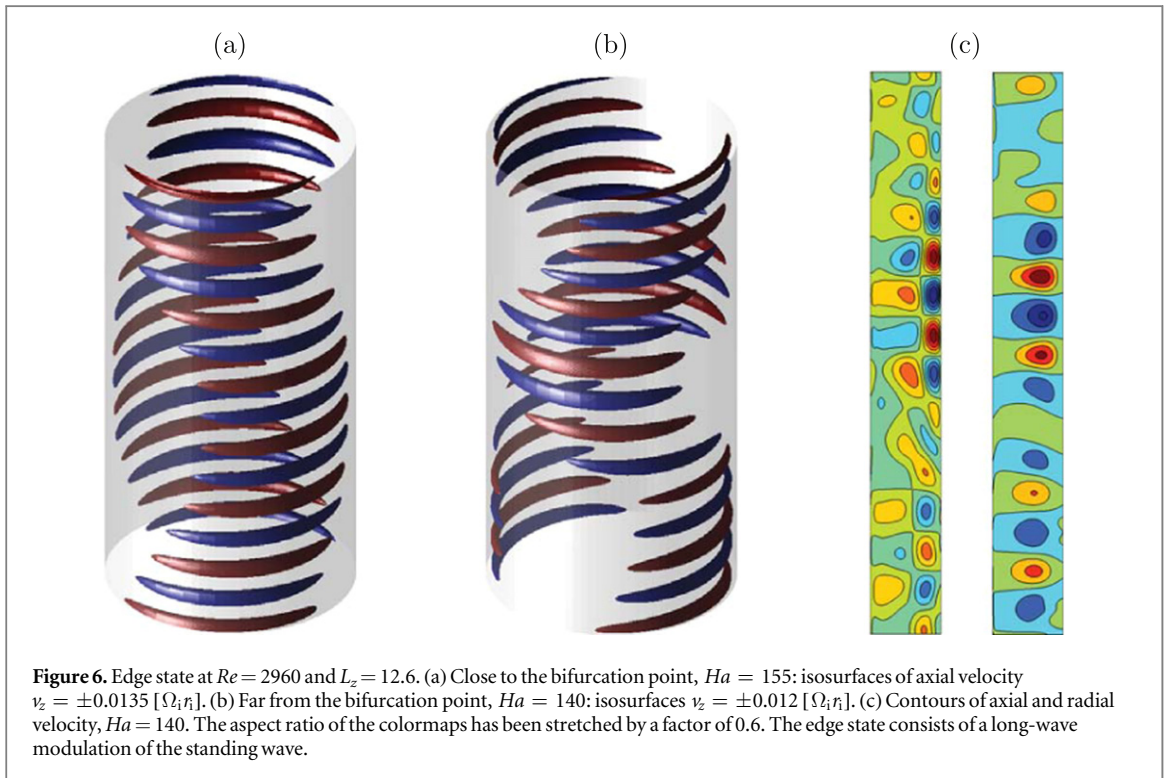
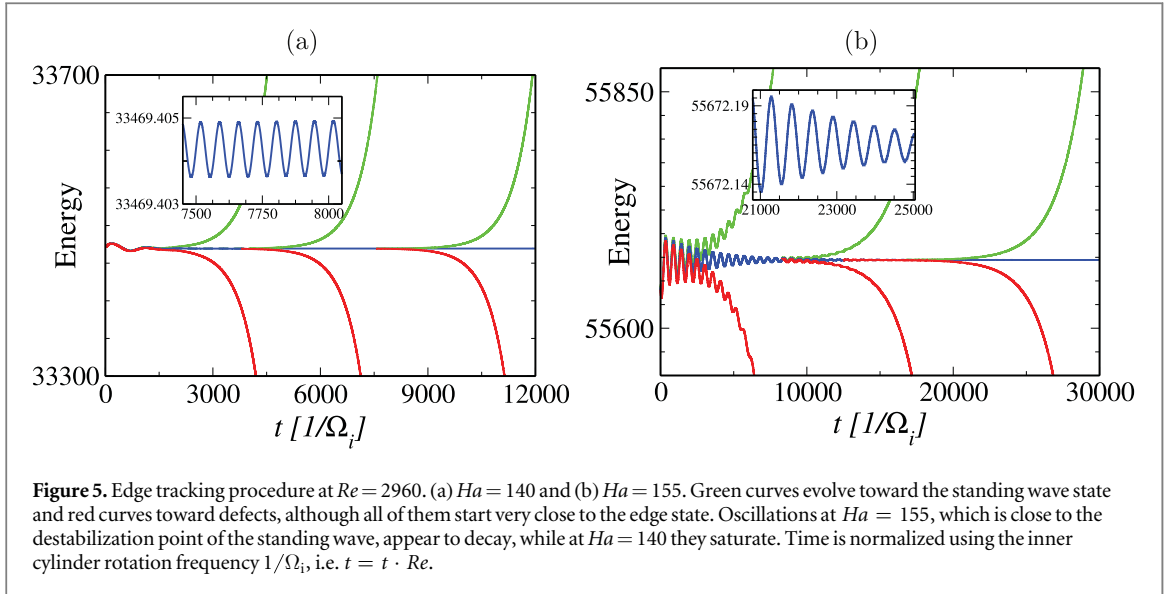
angular momentum. The maximum in torque correlates well with the maximum growth rate from the linear stability analysis shown in figure 3(b).

## 5. Onset of spatio-temporal chaos

At  $Re = 2960$  a Hopf bifurcation occurs at  $Ha_c = 120$  and the emerging SW remains stable until  $Ha = 160$ . Increasing  $Ha$  beyond this point a catastrophic transition to spatio-temporal chaos is observed: the vortex structure is damaged and the up–down symmetry is broken (figure 4). Between  $Ha = 130$  and 160 there is a hysteresis region in which both SW and spatio-temporal chaos (defects) are locally stable (see figure 3(a)). In this  $Ha$ -range, if the initial condition is a SW from another run with slightly different  $Ha$ , this remains stable. However, when starting for example from a randomly disturbed Couette profile the flow evolves directly to defects.

This catastrophic transition suggests a subcritical bifurcation. We investigated this hypothesis by computing the unstable branch separating defects and SW. For this purpose we combined time-stepping with a bisection strategy as follows. If the SW is slightly disturbed, then the flow should rapidly converge to the SW because it is locally stable. The same applies to defects. For intermediate initial conditions the flow should take a long time before asymptotically reaching either the SW or the defects. Such initial conditions were generated here by performing a linear combination between two selected flow snapshots of SW and defects. This combination was parametrized with a variable  $\beta$ , for which  $\beta = 0$  corresponds to SW and  $\beta = 1$  to defects. With the bisection procedure, refining  $\beta$  results in an initial condition successively closer to the manifold (or edge) delimiting the two basin boundaries. The edge is comprised of those initial conditions that tend neither to defects nor to SW, and the attractor in this manifold is referred to as an edge state [37].

Figure 5 shows that as initial conditions are taken closer to the edge, the temporal dynamics become simple as the edge state is approached. At  $Ha = 155$ , which is very close to the destabilization of the SW, the dynamics appear to exhibit a damped oscillation (see figure 5(b)). Unfortunately, it is difficult to establish whether the oscillation finally decays or saturates at a tiny amplitude, as expected close to the bifurcation point. At  $Ha = 140$ , however, which is further from the bifurcation point, the oscillation saturates at non-zero amplitude (see figure 5(a)). This suggests that the edge state is a relative periodic orbit (or modulated wave) emerging at a subcritical Hopf bifurcation of the SW. Despite this simple temporal behaviour, the spatial structure of the edge state is complicated (see figures 6(a)–(c)). It consists of a long-wave (subharmonic) modulation of the axially periodic pattern of the SW, which can be seen as a precursor to defects (compare figures 6(a) and (b) to 4(a)). We expect that as  $Ha$  is further reduced the edge state suffers a bifurcation cascade and becomes chaotic. This should



continuously connect to defects and stabilize at a turning point for  $Ha \gtrsim 130$ , which is the lowest  $Ha$  for which defects remain stable.

## 6. Turbulent transport of momentum

As the Reynolds number is further increased, defects are expected to grow gradually into turbulence. Although it would be very interesting to perform a two-parameter study of the dynamics in  $Ha$  and  $Re$ , this is computationally expensive and beyond the scope of the current work. We here chose to follow a parameter path of the form

$$Ha = a Re^b, \quad (26)$$

with  $a = 0.71$  and  $b = 1.55$ . This path is shown as a solid green line in figure 1(b) and provides a very good approximation to the curve of maximum growth rate of the linear stability analysis (red dashed line). It goes deep into the instability region and so we expect the instability to fully develop as  $Re$  increases with  $Ha$  subject to (26).

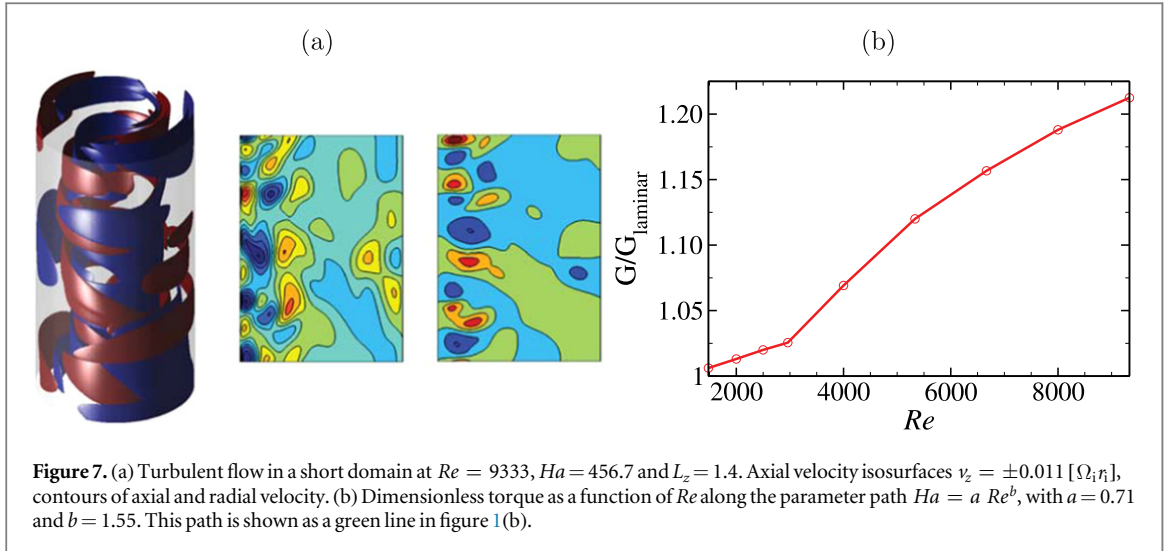


**Figure 7.** (a) Turbulent flow in a short domain at  $Re = 9333$ ,  $Ha = 456.7$  and  $L_z = 1.4$ . Axial velocity isosurfaces  $v_z = \pm 0.011 [\Omega_i r_i]$ , contours of axial and radial velocity. (b) Dimensionless torque as a function of  $Re$  along the parameter path  $Ha = a Re^b$ , with  $a = 0.71$  and  $b = 1.55$ . This path is shown as a green line in figure 1(b).

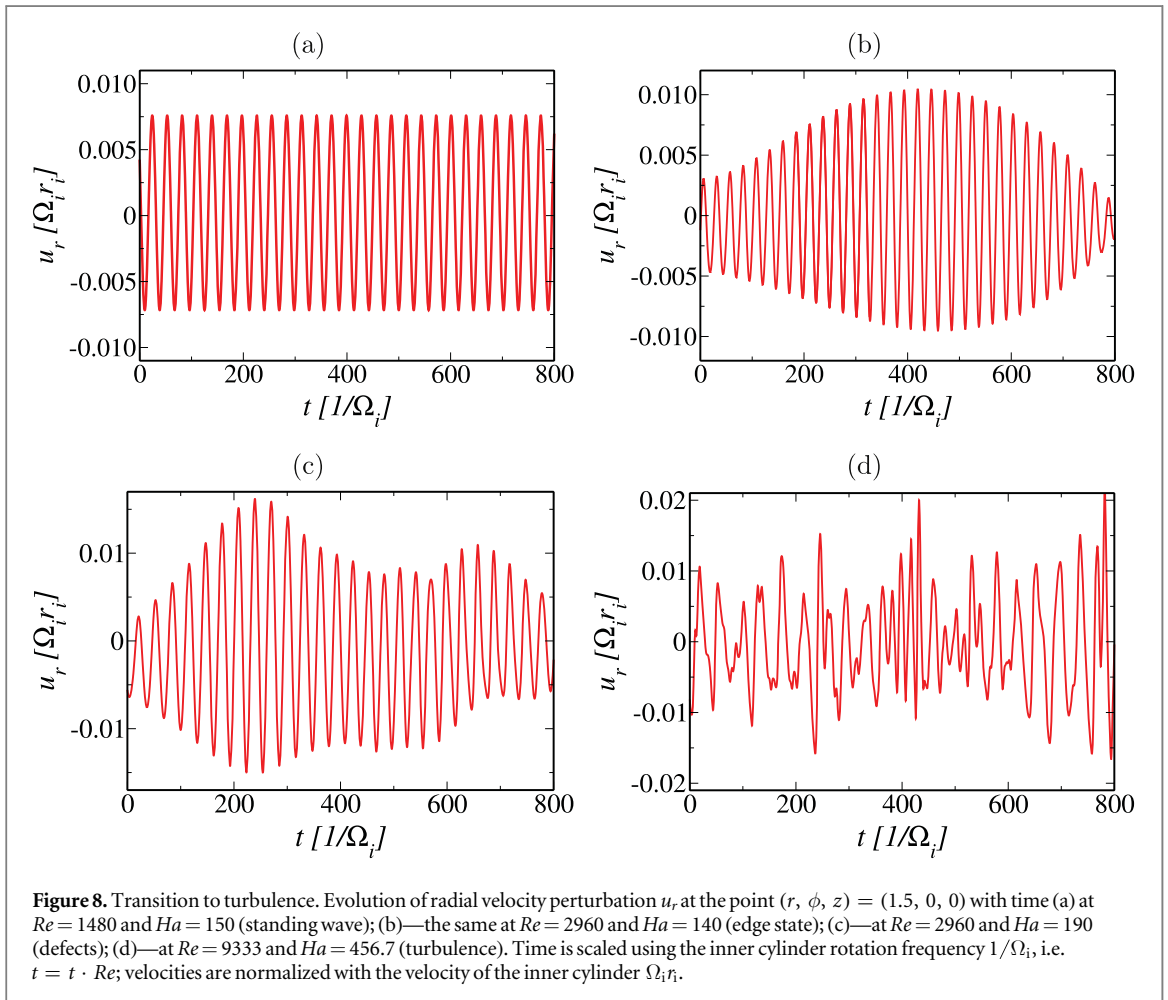
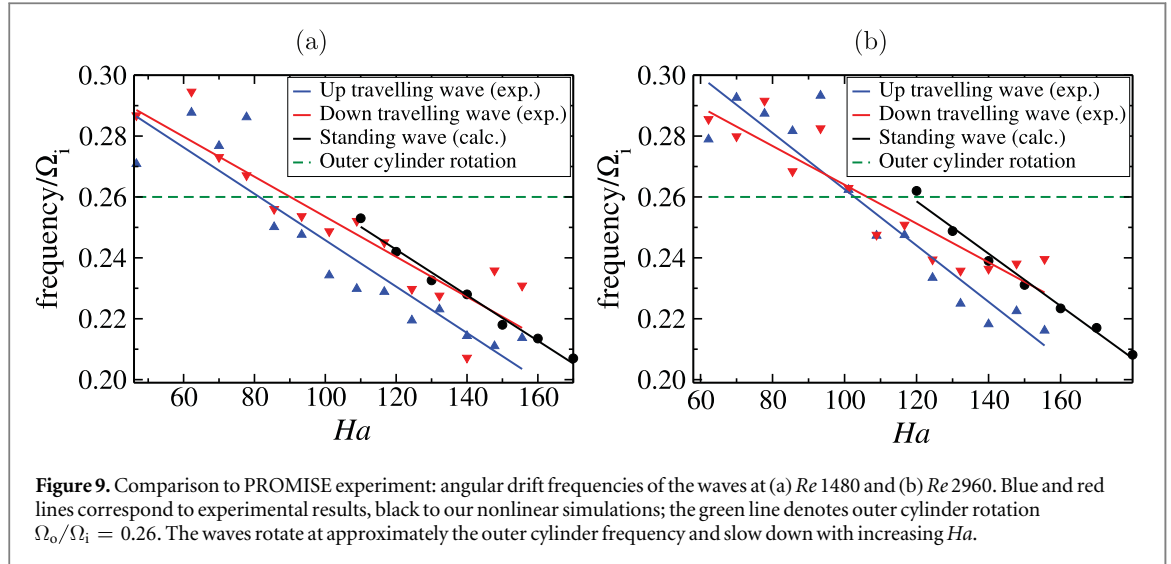


**Figure 8.** Transition to turbulence. Evolution of radial velocity perturbation  $u_r$  at the point  $(r, \phi, z) = (1.5, 0, 0)$  with time (a) at  $Re = 1480$  and  $Ha = 150$  (standing wave); (b)—the same at  $Re = 2960$  and  $Ha = 140$  (edge state); (c)—at  $Re = 2960$  and  $Ha = 190$  (defects); (d)—at  $Re = 9333$  and  $Ha = 456.7$  (turbulence). Time is scaled using the inner cylinder rotation frequency  $1/\Omega_i$ , i.e.  $t = t \cdot Re$ ; velocities are normalized with the velocity of the inner cylinder  $\Omega_i r_i$ .

At  $Re = 4000$  the vortices are small at the inner cylinder and remain quite large at the outer cylinder (figure 4(b)), and at  $Re = 9333$  this tendency develops into rapidly drifting small vortices at the inner cylinder and slow large vortices at the outer cylinder (figure 7(a)). There is no preferred direction in the system; vortices can travel up or down, both at the inner and outer cylinders.

The qualitative difference between SW, defects and turbulent flow is apparent in time series of the radial velocity  $v_r$  taken at the mid-gap between the cylinders  $(r, \phi, z) = (1.5, 0, 0)$ . Figure 8(a) shows that the radial velocity of the SW oscillates periodically around zero. The edge state features a slow temporal frequency modulating the oscillation of the SW (figure 8(b)). For defects at  $Re = 2960$  the time series is mildly chaotic. As



$Re$  increases toward turbulence the velocity pulsates in a very chaotic manner (figure 8(d)). However, the main frequency associated with the AMRI can still be discerned. By comparing all panels it becomes apparent that this frequency scales with the rotation-rate of the inner cylinder. This is consistent with the linear stability analysis of [8], and with the studies [38, 39], where it is shown that in the low  $Pm$  limit the AMRI is an inertial wave.

The transfer-rate of angular momentum between the cylinders is important for accretion-disc modelling. We checked the torque scaling for increasing  $Re$  numbers (see figure 7(b)) along the parameter path (26). The dimensionless torque increases with  $Re$  according to the scaling law

$$G \sim Re^{1.15}, \quad (27)$$

which is surprisingly low compared to hydrodynamic experiments in the Rayleigh unstable regime [40]. We believe that this torque scaling comes close to being an upper bound for the torque scaling of the AMRI in the  $Re$  range studied here because the maximum in torque correlates well with maximum growth rates at low  $Re$  (see figure 3). However, we must caution that in hydrodynamic Taylor–Couette flow different maxima of the torque have been observed as a function of the relative rotation of the cylinders [41]. At large  $Re$  these are not correlated to the maximum growth rate of the primary instability. Similar phenomena may occur for the AMRI.

## 7. Discussion

We showed that the AMRI in Taylor–Couette flow manifests itself as a wave rotating in the azimuthal direction and standing in the axial direction, thereby preserving the reflection symmetry in the latter. In order to compare to experimental observations [17] we computed the angular drift frequency of the wave. This is shown in figure 9 after being normalized with the rotation frequency of the inner cylinder. The wave rotates at approximately the outer cylinder frequency (dashed line) and slows down as the Hartmann number increases, which is in qualitative agreement with the experimental data. Note, however, that in the experiment two frequencies are simultaneously measured, corresponding to the up- and down-traveling spiral waves, respectively. Although in the SW the two frequencies are identical, in the experiment the asymmetric wiring creates  $B_r$  and  $B_z$  components of magnetic field which break the reflectional symmetry. As a result, up and down spirals travel with different frequencies, similar to co-rotating Taylor–Couette flow in which the reflection symmetry is broken by an imposed axial flow [42]. Another difference is that in the experiment the flow becomes unstable at lower  $Ha$ , which may be explained by the different boundary conditions in the experiment from our simulations. In the experiment copper cylinders are used, so perfectly conducting walls would be a closer boundary condition for the magnetic field. More significantly, in the experiments the cylinders are of finite length, so to reproduce their results exactly a no-slip condition on end-plates should be used. We have applied periodic boundary conditions in the axial direction, which more accurately model the accretion disc problem and allow us to compute high Reynolds number flows more efficiently.

As  $Re$  increases, a catastrophic transition to spatio-temporal chaos occurs directly from the SW. In a range of parameters SW and chaos are both locally stable and can be realized depending on the initial conditions. We have shown that the first step in this transition process is a subcritical Hopf bifurcation giving rise to an unstable relative periodic orbit, which has been computed using an analogue of the edge-tracking algorithm introduced by Skufca et al [37] in shear flows. This unstable relative periodic orbit consists of a long-wave modulation of the

axially periodic pattern of the SW and destroys the homogeneity of the vortical pattern. It can thus be seen as a temporally simple defect precursor of the ensuing spatio-temporal chaos. Because of the computational cost we could not track further instabilities on the unstable branch, which we speculate result in chaotic flow before the dynamics stabilize at a turning point ( $Ha = 130$  at  $Re = 2960$ ). After the turning point defects are stable and can be computed simply by time-stepping.

We believe that such long-wave instabilities are ubiquitous in fluid flows. In linearly stable shear flows, such instabilities of TWs were found to be responsible for spatial localization [43, 44]. In fact, in pipe flow the ensuing localized solutions, which are also relative periodic orbits, suffer a bifurcation cascade leading to chaos [45]. One difference is that in pipe flow the TWs are disconnected from laminar flow, where the SW of the AMRI is connected to the circular Couette flow.

Our simulations were performed with a powerful spectral DNS method, which we have developed and validated with published results to excellent agreement. The method allowed us to compute flows up to  $Re = 10^4$ . As  $Re$  increases, defects accumulate and the flow becomes gradually turbulent. Although we found that the AMRI exhibits a weak scaling of angular momentum transport, with  $G \propto Re^{1.16}$ , we expect that larger magnetic Prandtl numbers  $Pm$  (realistic for accretion discs) may result in a stronger scaling. Astrophysically important issues such as the precise angular momentum transport scalings obtained for different values of  $Pm$ , and also for different choices of imposed field (e.g. SMRI, HMRI, AMRI) will be the subject of future investigations.

## Acknowledgments

Support from the Deutsche Forschungsgemeinschaft (grant number AV 120/1-1) and computing time from the Jülich Supercomputing Centre (grant number HER22) and Regionales Rechenzentrum Erlangen (RRZE) are acknowledged.

## References

- [1] Velikhov E 1959 Stability of an ideally conducting liquid flowing between rotating cylinders in a magnetic field *Zh. Eksp. Teor. Fiz.* **36** 1398–404
- [2] Balbus S A and Hawley J F 1991 A powerful local shear instability in weakly magnetized disks *Astrophys. J.* **376** 214–33
- [3] Shakura N and Sunyaev R 1973 Black holes in binary systems. Observational appearance *Astron. Astrophys.* **24** 337–55
- [4] Rayleigh L 1917 On the dynamics of revolving fluids *Proc. R. Soc.* **148**–54
- [5] Ogilvie G and Pringle J 1996 The non-axisymmetric instability of a cylindrical shear flow containing an azimuthal magnetic field *Mon. Not. R. Astron. Soc.* **279** 152–64
- [6] Balbus S A and Hawley J F 1998 Instability, turbulence, and enhanced transport in accretion disks *Rev. Mod. Phys.* **70** 1
- [7] Hollerbach R and Rüdiger G 2005 New type of magnetorotational instability in cylindrical Taylor–Couette flow *Phys. Rev. Lett.* **95** 124501
- [8] Hollerbach R, Teeluck V and Rüdiger G 2010 Nonaxisymmetric magnetorotational instabilities in cylindrical Taylor–Couette flow *Phys. Rev. Lett.* **104** 044502
- [9] Umurhan O, Menou K and Regev O 2007 Weakly nonlinear analysis of the magnetorotational instability in a model channel flow *Phys. Rev. Lett.* **98** 034501
- [10] Ji H, Goodman J and Kageyama A 2001 Magnetorotational instability in a rotating liquid metal annulus *Mon. Not. R. Astron. Soc.* **325** 1–5
- [11] Rüdiger G and Zhang Y 2001 MHD instability in differentially-rotating cylindrical flows *Astron. Astrophys.* **378** 302–8
- [12] Edlund E M and Ji H 2014 Nonlinear stability of laboratory quasi-Keplerian flows *Phys. Rev. E* **89** 021004
- [13] Avila M 2012 Stability and angular-momentum transport of fluid flows between corotating cylinders *Phys. Rev. Lett.* **108** 124501
- [14] Nordsiek F, Huisman S G, van der Veen R C, Sun C, Lohse D and Lathrop D P 2014 Azimuthal velocity profiles in Rayleigh-stable Taylor–Couette flow and implied axial angular momentum transport arXiv:1408.1059
- [15] Stefani F, Gundrum T, Gerbeth G, Rüdiger G, Schultz M, Szklarski J and Hollerbach R 2006 Experimental evidence for magnetorotational instability in a Taylor–Couette flow under the influence of a helical magnetic field *Phys. Rev. Lett.* **97** 184502
- [16] Stefani F, Gerbeth G, Gundrum T, Hollerbach R, Priede J, Rüdiger G and Szklarski J 2009 Helical magnetorotational instability in a Taylor–Couette flow with strongly reduced Ekman pumping *Phys. Rev. E* **80** 066303
- [17] Seilmayer M, Galindo V, Gerbeth G, Gundrum T, Stefani F, Gellert M, Rüdiger G, Schultz M and Hollerbach R 2014 Experimental evidence for nonaxisymmetric magnetorotational instability in a rotating liquid metal exposed to an azimuthal magnetic field *Phys. Rev. Lett.* **113** 024505
- [18] Chandrasekhar S 1961 *Hydrodynamic and Hydromagnetic Stability* (New York: Dover)
- [19] Willis A P and Barenghi C F 2002 Hydromagnetic Taylor–Couette flow: numerical formulation and comparison with experiment *J. Fluid Mech.* **463** 361–75
- [20] Crawford J D and Knobloch E 1991 Symmetry and symmetry-breaking bifurcations in fluid dynamics *Ann. Rev. Fluid. Mech.* **23** 341–87
- [21] Knobloch E 1996 Symmetry and instability in rotating hydrodynamic and magnetohydrodynamic flows *Phys. Fluids* **8** 1446–54
- [22] Hollerbach R 2008 Spectral solutions of the MHD equations in cylindrical geometry *Int. J. Pure Appl. Math.* **42** 575
- [23] Moser R D, Moin P and Leonard A 1983 A spectral numerical method for the Navier–Stokes equations with applications to Taylor–Couette flow *J. Comput. Phys.* **52** 524–44
- [24] Meseguer A, Avila M, Mellibovsky F and Marques F 2007 Solenoidal spectral formulations for the computation of secondary flows in cylindrical and annular geometries *Eur. Phys. J. Spec. Top.* **146** 24–259

- [25] Shi L, Rampf M, Hof B and Avila M 2015 A hybrid MPI-openMP parallel implementation for pseudospectral simulations with application to Taylor–Couette flow *Comput. Fluids* **106** 1–11
- [26] Rempfer D 2006 On boundary conditions for incompressible Navier–Stokes problems *Appl. Mech. Rev.* **59** 107–25
- [27] Marcus P S 1984 Simulation of Taylor–Couette flow: I. Numerical methods and comparison with experiment *J. Fluid Mech.* **146** 45–64
- [28] Brackbill J U and Barnes D 1980 The effect of nonzero  $\nabla \cdot B$  on the numerical solution of the magnetohydrodynamic equations *J. Comput. Phys.* **35** 426–30
- [29] Ramshaw J D 1983 A method for enforcing the solenoidal condition on magnetic field in numerical calculations *J. Comput. Phys.* **52** 592–6
- [30] Frigo M and Johnson S G 2005 The design and implementation of fftw3 *Proc. IEEE* **93** 216–31
- [31] Lawson C L, Hanson R J, Kincaid D R and Krogh F T 1979 Basic linear algebra subprograms for fortran usage *ACM Trans. Math. Softw. (TOMS)* **5** 308–23
- [32] Anderson E et al 1999 *LAPACK Users' Guide* 3rd edn (Philadelphia, PA: Society for Industrial and Applied Mathematics)
- [33] Roberts P 1964 The stability of hydromagnetic Couette flow *Proc. Cambridge Philosophical Society* vol 60 (Williams Bay, WA: Yerkes Observatory)
- [34] Willis A P and Barenghi C F 2002 Magnetic instability in a sheared azimuthal flow *Astron. Astrophys.* **388**
- [35] Willis A P and Barenghi C F 2002 A Taylor–Couette dynamo *Astron. Astrophys.* **393** 339–43
- [36] Riecke H and Paap H-G 1986 Stability and wave-vector restriction of axisymmetric Taylor vortex flow *Phys. Rev. A* **33** 547
- [37] Skufca J D, Yorke J A and Eckhardt B 2006 Edge of chaos in a parallel shear flow *Phys. Rev. Lett.* **96** 174101
- [38] Kirillov O N and Stefani F 2010 On the relation of standard and helical magnetorotational instability *Astrophys. J.* **712** 52
- [39] Kirillov O N, Stefani F and Fukumoto Y 2012 A unifying picture of helical and azimuthal magnetorotational instability, and the universal significance of the liu limit *Astrophys. J.* **756** 83
- [40] Lathrop D P, Fineberg J and Swinney H L 1992 Turbulent flow between concentric rotating cylinders at large Reynolds number *Phys. Rev. Lett.* **68** 1515
- [41] Brauckmann H J, Salewski M and Eckhardt B 2015 Momentum transport in Taylor–Couette flow with vanishing curvature arXiv:1505.06278
- [42] Avila M, Meseguer A and Marques F 2006 Double Hopf bifurcation in corotating spiral Poiseuille flow *Phys. Fluids* **18** 064101
- [43] Melnikov K, Kreilos T and Eckhardt B 2014 Long-wavelength instability of coherent structures in plane Couette flow *Phys. Rev. E* **89** 043008
- [44] Chantry M, Willis A P and Kerswell R R 2014 Genesis of streamwise-localized solutions from globally periodic traveling waves in pipe flow *Phys. Rev. Lett.* **112** 164501
- [45] Avila M, Mellibovsky F, Roland N and Hof B 2013 Streamwise-localized solutions at the onset of turbulence in pipe flow *Phys. Rev. Lett.* **110** 224502